Sensors & Actuators: A. Physical 359 (2023) 114475

Contents lists available at ScienceDirect

Sensors and Actuators: A. Physical

journal homepage: www.journals.elsevier.com/sensors-and-actuators-a-physical

# Real-time 3D plane-wave imaging using annular capacitive micromachined ultrasonic transducer array

Young Seok Kwon [a,b], Hae Youn Kim [a], Dong-Hyun Kang [a], Dong Hun Kim [a], Jae-Woong Jeong [b,*], Byung Chul Lee [a,c,d,**]

[a] Bionics Research Center, Korea Institute of Science and Technology (KIST), Seoul 02792, Republic of Korea
[b] School of Electrical Engineering, Korea Advanced Institute of Science and Technology, Daejeon 34141, Republic of Korea
[c] Division of Bio-Medical Science & Technology, KIST School, University of Science & Technology (UST), Seoul 02792, Republic of Korea
[d] KHU-KIST Department of Converging Science and Technology, Kyung Hee University, Seoul 02447, Republic of Korea

ARTICLE INFO

*Keywords:*
Plane-wave imaging
3D real-time ultrasonography
Annular capacitive micromachined ultrasonic transducer
Sparse array
Wafer bonding

ABSTRACT

Imaging methods and 2D sparse arrays have been extensively researched to realize real-time 3D volumetric imaging with higher frame rates. In this study, we developed a 3D plane-wave imaging method using an annular capacitive micromachined ultrasonic transducer (CMUT) array as a breakthrough technique for realizing 3D imaging with a limited number of elements. We adopted the double oxidation and wafer bonding processes for creating the cavity of a CMUT with a 2 μm silicon membrane. To ensure surface uniformity before the bonding process, we implemented an additional reactive ion etching process after the second oxidation. The characterization results showed that the resonant frequency of the proposed device was 6.2 MHz with 65 V collapse voltage. The demonstration of real-time 3D volumetric imaging was conducted in oil using a Vantage 64 ultrasound research system. A plane-wave imaging scheme was used to detect wire phantoms immersed in the oil, with 289 plane waves transmitted over a range of 20° from the center of the annular array. The reconstructed data were used to create three orthogonal cross sections of the target region. The − 6 dB lateral and axial resolutions were 0.56 mm and 0.35 mm for the wires positioned at 18 mm from the proposed device, which were narrow enough to detect a wire phantom of 380 μm diameter. The normalized frame rate was calculated and compared with that in a previous study. We verified that plane-wave imaging has advantages in real-time imaging when compared with the classic phased array and synthetic phased array. Thus, the annular CMUT array is a promising mechanism for real-time 3D imaging with higher frame rate than that possible with previous methods.

## 1. Introduction

Medical ultrasonography is widely used in clinical practice owing to its advantages of non-invasiveness, low-cost, and non-ionizing radiation when compared with computed tomography and magnetic resonance imaging. In addition, the fast data acquisition rate of ultrasonography supports its application in real-time 3D imaging. However, the conventional 1D array transducer can acquire only 2D ultrasound images, resulting in misdiagnoses due to the inability to detect and identify certain features. Although it is possible for a 1D array transducer to obtain volumetric data via mechanical scanning, this method is unsuitable for real-time imaging owing to its low data acquisition rate [1–3]. Various types of 2D array transducers have been proposed for 3D ultrasound imaging [4–8]. The 2D matrix array, which is the most conventional 2D ultrasound transducer, provides vivid 3D ultrasound images. However, the large number of elements required for high-quality 3D ultrasound images necessitates numerous interconnections during fabrication, thus increasing the system complexity and cost. It also increases the computational load, making it difficult to realize real-time 3D imaging.

Two-dimensional sparse arrays with low systemic load were proposed to ensure a sufficiently low computational load for reconstruction of real-time 3D images. Unlike the conventional bulk-piezoelectric transducers produced via blade dicing, capacitive micromachined

* Corresponding author.
** Corresponding author at: Bionics Research Center, Korea Institute of Science and Technology (KIST), Seoul 02792, Republic of Korea.
*E-mail addresses:* jjeong1@kaist.ac.kr (J.-W. Jeong), bclee@kist.re.kr (B.C. Lee).

https://doi.org/10.1016/j.sna.2023.114475
Received 6 February 2023; Received in revised form 13 May 2023; Accepted 5 June 2023

ultrasonic transducers (CMUTs) have no geometrical limitation owing to their ease of microfabrication using semiconductor fabrication techniques. Hence, CMUTs have superior features that support fabrication of sparse arrays. Because CMUT fabrication utilizes silicon, it is lead-free; moreover, it is suitable for smaller cell-to-cell distances, which is essential for lowering the grating lobes in ultrasonography. The advantages of wide bandwidth, low fabrication cost, and relative ease of miniaturization have spurred the development of CMUTs with various types of arrays [1,9–11].

The annular array, which is a type of sparse array, has been recommended for various applications of multi-modal medical therapy and imaging, such as photoacoustics and integration with other implantable devices. The ease of microfabrication has facilitated the shrinking of the annular CMUT array, allowing its application to small catheters for capillaries. The annular CMUT array combined with the catheter can be used in various applications ranging from catheter guidance to radio frequency laser ablation of the target tissue. Thus, the annular CMUT array is a representative sparse array for 3D imaging [12–14].

To realize 3D imaging with a CMUT array, it is essential to select the appropriate imaging method by considering the device geometry and wave property. Although real-time 3D imaging with a sparse array using conventional beamforming methods is available simply by changing the probe geometry definition, its system is complex. Synthetic beamforming is one of the good candidates to realize 3D ultrasound imaging with low systemic complexity and load. The classic phased array (CPA) is a widely used imaging scheme that involves firing multiple focused beams at different angles via beam steering. In real-time imaging, the repeated transmissions lower the data transfer rate, which deteriorates the imaging quality. As an alternative to CPA imaging, a synthetic phased array (SPA) imaging method that applies Hadamard coding and multiplicative weighting scheme to each pair of transmitting and receiving elements was developed in a previous study [15]. However, this method has lower signal-to-noise ratio (SNR) and higher computational load than CPA imaging. Real-time 3D imaging requires high data acquisition rate, low computational load, and sufficient SNR.

This paper presents a plane-wave 3D imaging scheme that uses an annular CMUT array as a breakthrough method for real-time 3D imaging with low systemic load. Plane-wave ultrasound imaging is able to achieve ultrafast ultrasound imaging compared with conventional focused ultrasound imaging, which demonstrates its advantages over the synthetic aperture (SPA) method in signal-to-noise ratio (SNR) and penetration depth [16]. Despite plane-wave facilitating ultrafast ultrasound imaging, there is no report that applied in real-time 3D ultrasound imaging to our best knowledge. In this paper, we adopted a plane-wave ultrasound imaging scheme to achieve real-time 3D ultrasound images via an annular CMUT array, which configuration provides advantages in beamforming and imaging performance of real-time 3D ultrasound imaging. The conceptual schematic of the proposed annular CMUT array and the real-time 3D imaging are shown in Fig. 1. The method involves transmitting 289 plane waves, each of which is steered along two planes orthogonal to the transducer surface over a range of 20° from the center of the annular array. The number of transmissions is lower than that in CPA imaging, and no additional weighting factors are multiplied. Real-time 3D imaging was demonstrated using different configurations of wire phantoms. The results showed that the YZ- and XY-plane of the target region were successfully reconstructed.

**Table 1**
Physical parameters of the annular CMUT array.

| Design Parameter | |
|---|---|
| Array diameter (mm) | 9.46 |
| Cell diameter (μm) | 52 |
| Gap height (nm) | 145 |
| Insulator thickness (μm) | 0.23 |
| Moving plate thickness (μm) | 2 |
| Electrode (Al) thickness (μm) | 0.5 |
| Target resonant frequency (MHz) | 6.7 |
| Number of elements used in imaging (pair) | 50 |
| Internal ring diameter (mm) | 7.8 |
| Dimension of each elements (μm) | 200 × 260 |
| Pitch of elements (μm) | 124 |

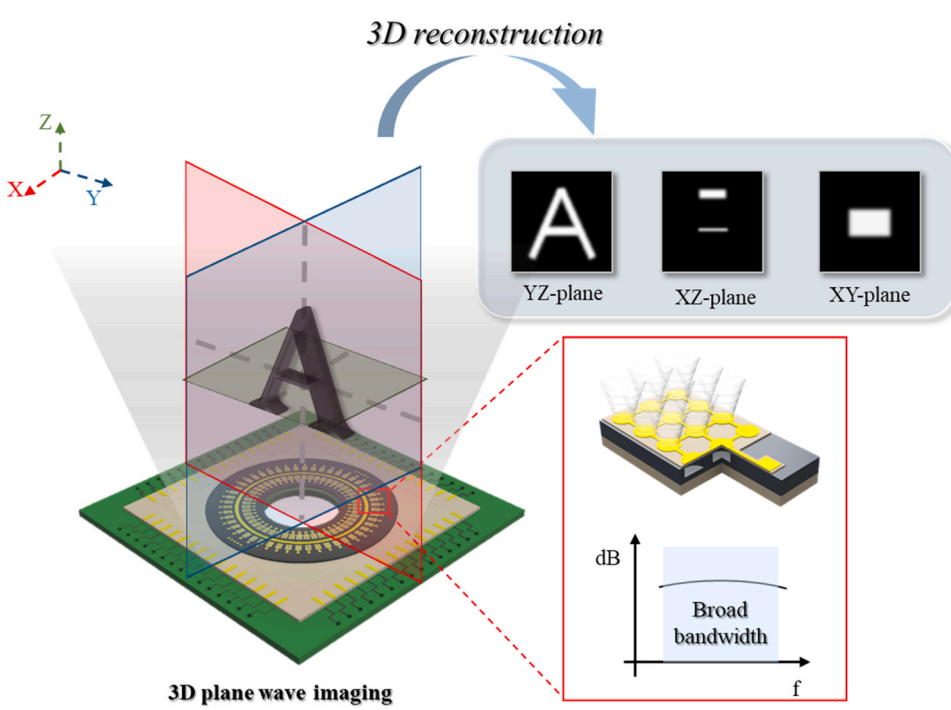


**Fig. 1.** Conceptual schematic of annular CMUT array for medical ultrasonography.

## 2. Design and fabrication

### 2.1. Design of annular CMUT

Table 1 shows the design parameters of the annular CMUT array. The diameter of the cells in the array is 52 μm, targeting a resonant frequency of 6.7 MHz in oil. Each element consists of 12 cells, and the thickness of the moving plate is 2 μm. The distance between the elements is approximately 250 μm, which is slightly higher than 1/2 the wavelength of the wave at 6.7 MHz, i.e., the target resonant frequency of the outer array element [17,18].

### 2.2. Fabrication and structure of dual annular CMUT array

To fabricate the proposed dual annular CMUT, we selected the wafer bonding method for more enhanced characterization than that achieved with the sacrificial release method. Specifically, the wafer bonding method ensures equivalent operating conditions for all elements, which is important for forming the ideal ultrasound wave. Some previous studies adopted the sacrificial layer release method, which deposits the membrane layer on the sacrificial layer [19,20]. However, the method has critical issues such as stiction, intrinsic stress in the nitride layer, and unreliable membrane layer, which affect the resonance frequency of the cell [21,22]. In this study, the CMUT was fabricated according to the following process. First, as shown in Fig. 2(a), the 200-nm-thick silicon dioxide layer was grown through dry oxidation in a furnace at 1070 °C to define the vacuum cavity that was wet etched using buffered oxide etchant (BOE). To create an insulating layer, a second but briefer oxidation process was conducted in the furnace at 1070 °C (Fig. 2(b)). After the second oxidation, the cavity depth was measured as 145 nm using a stylus profiler (Alpha step IQ, KLA-TENCOR, USA). Next, a silicon-on-insulator (SOI) wafer, a prime four-inch SOI wafer with a highly doped (<0.005 Ω·cm) device layer of 2 μm thickness, was bonded to the fabricated wafer under high vacuum conditions with pressure under $10^{-5}$ mbar (Fig. 2(c)). Then, the handling layer and buried oxide layer were released through wet etching using KOH solution mixed with deionized water, potassium hydroxide pellet (purchased from DAEJUNG Chemicals and Metal, Republic of Korea), and 6:1 BOE (purchased from SAMCHUN chemicals, Republic of Korea) (Fig. 2(d)). To define the top moving plate and allow electrical contact, we used conventional photolithography and reactive ion etching (RIE) to expose the bottom silicon (Fig. 2(e)). Finally, a thin layer of Al (500 nm) was deposited and etched using a sputtering system (SME-200, ULVAC, Japan) and Al etchant (aluminum etchant type A, purchased from DAEJUNG Chemicals and Metal, Republic of Korea); in addition, a Au pad was deposited and patterned using an e-beam evaporation system (E-beam evaporator, ULVAC, Japan) and lift-off process (Fig. 2(f)). We used deep trench RIE in the last step to achieve singulation of the proposed device. The void at the center can be utilized for integration with various medical devices such as intracardiac catheter and photoacoustic device, which needs extra space for the laser emitter.

Fig. 3(a) shows the photographs of an annular CMUT array. The small size of the CMUT array (less than a quarter of the area of a one euro coin) grants advantages when combined with a small-size catheter. The size of a single element in the annular CMUT array was 200 × 260 μm, as shown in Fig. 3(b). Fig. 3(c) shows the scanning electron microscope (SEM) image of the CMUT cell. The vacuum gap between the insulating oxide layer and the membrane was 146 nm, which agrees with the data

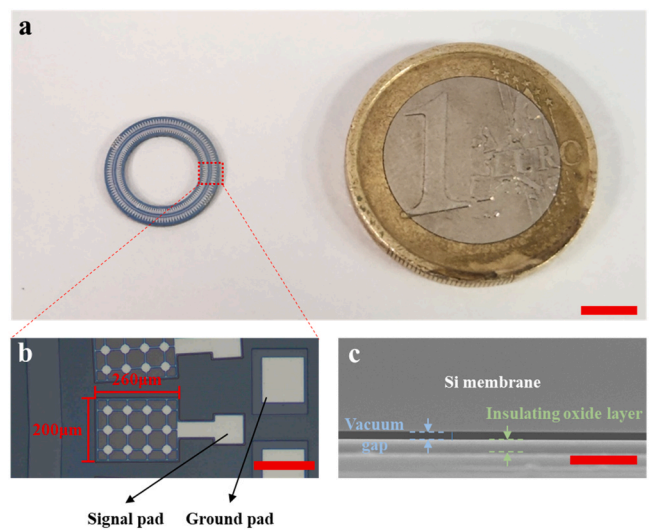


**Fig. 3.** Dimensions of annular CMUT array. (a) Comparison of the proposed device and 1 € coin. Scale bar is 5 mm. (b) OM image of single element and ground pad. Scale bar is 200 μm. (c) SEM image of CMUT cell. The vacuum gap and insulating oxide layer are 146 nm and 234 nm thick, respectively. Scale bar is 1 μm.

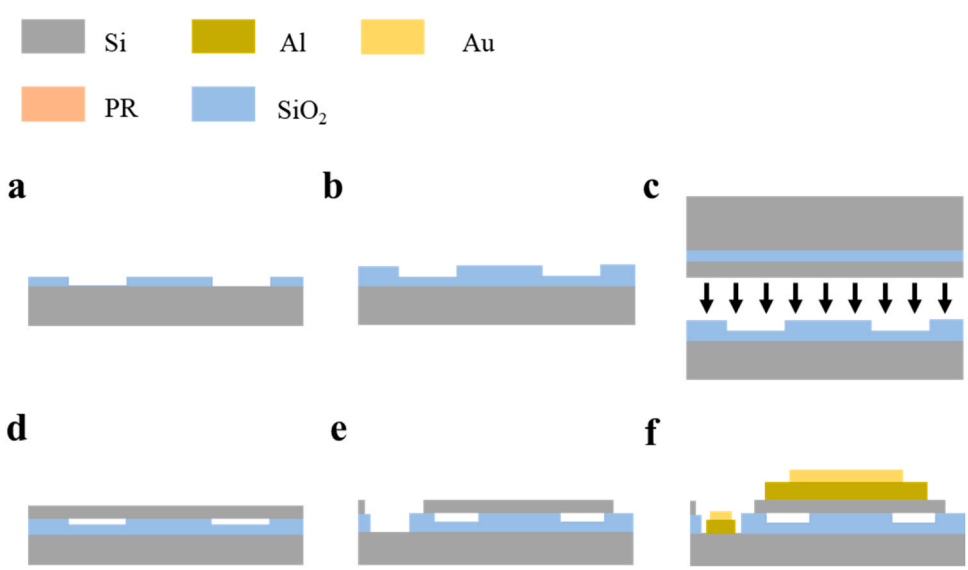


**Fig. 2.** Fabrication process of annular CMUT array. (a) Cavity patterning before second oxidation. (b) After second oxidation. (c) Wafer bonding process. (d) Handling layer release. (e) Si membrane isolation and grounding via patterning using RIE. f) Al electrode and Au pad patterning.

from the stylus profiler mentioned earlier. The insulating oxide layer thickness was 234 nm.

### 2.3. Circuit system for device

Because applying the DC bias and AC signal to the individual CMUT element is essential for characterization and demonstration of the CMUT, we designed a homemade circuit board, as shown in Fig. 4(a). We grouped 120 elements in 2:1 ratio to create 60 channels to interface with a Vantage 64 ultrasound research system (Vantage 64, Verasonics Inc., USA). We applied PIN diode switches (GF-124–0013, C&K, USA) to all 120 elements to control each element individually. As shown in Fig. 4 (b), the SP3T switch allows each channel to be independently controlled for connection with external devices, and the SMA connector is used to apply AC and DC signals to the device for laser Doppler vibrometer (LDV) or hydrophone measurements. Additionally, a ground terminal is available to prevent unexpected leakage due to malfunctioning elements. A notable aspect of this PCB is the route of the interconnecting line for each element. A large board is required to arrange 60 groups of elements. This causes a difference in the interconnecting lines among the groups, resulting in an RC delay for each group, which impairs the image quality. To prevent the RC delay, we set the deviation of the line to lower than 10% of the median.

## 3. Characterization

### 3.1. Impedance measurement

To obtain the electrical characteristics of the proposed device, we evaluated the resonance frequency and collapse voltage using an impedance analyzer (DSO-X 2004A, Keysight Technology Inc., USA). A DC bias was applied to the device by electrically connecting a DC supply (PS310 high-voltage power supply, Stanford research systems Inc., USA), impedance analyzer, and the device using a bias-T. Fig. 5 shows the measured impedances at various DC bias voltages. It can be seen that the lowest resonant mode appears at 9.76 MHz with 30 V of DC bias. As the DC bias increases, the resonance peak appears at a lower frequency owing to the spring-softening effect [18]. When collapse occurs, the resonance peak moves to a higher frequency [23]. From Fig. 5, we found that the resonant peak disappeared in the range of 4–15 MHz when the DC bias exceeded 65 V. Thus, we concluded that the collapse voltage was 65 V and the proper operating DC bias was approximately 50 V, i.e., 80% of the collapse voltage.

### 3.2. Surface deflection measurement

The LDV can detect nano-scale motions using the time difference between the transmitted and received laser beams. Because the device is operated at the resonant frequency, the mode shape of the cells may vary depending on the bonding quality of the corresponding area. To ensure that all cells were activated in the first mode, we scanned one element in the array with an LDV (OFV-2570, Polytec Inc., USA) and small XYZ-motor (KDC101, Thorlabs Inc., USA). Fig. 6(a) depicts the schematic of the LDV measurement setup. The annular CMUT array was immersed in oil and connected to a DC supply and function generator (33500B series, Keysight Technology Inc., USA). We applied a 25 V DC bias and 7 $V_{pp}$ AC sine wave at the 6.2 MHz resonant frequency to one element in the device while every other element was connected to the ground terminal. The step size of the scanning motor was 4 μm and number of scanning points was 10,201, which corresponded to 101 × 101 points, resulting in a 400 × 400 μm scanning region. Fig. 6(b) shows the result of the raster scan. The topography of the element shows that all cells in the element were activated in the first mode. As the device is immersed in oil, electrical crosstalk vibrates the cells in the elements connected to the ground terminal. However, Fig. 6(b) shows that the amplitude of this interference is negligible when compared with that of the element applied with DC bias. In addition, the 12 cells in the same element showed phase differences. As the top electrode and connecting line were fabricated using the aluminum etchant, we believe that the increased line resistance due to the over-etched electrode caused these phase differences. Variations in the bonding quality of the cells may also contribute to phase differences, although we were unable to inspect each cell individually. We suppose this may affect the array's performance and introduce some degree of variability in the resulting images.

### 3.3. Pulse response measurement using hydrophone

The impulse response of the annular CMUT array, which contains information such as acoustic pressure, bandwidth, attenuation, and length of the signal, was measured using a hydrophone (HGL-0200, ONDA Corporation, USA). As the length of the impulse signal is a significant factor that determines the axial resolution, it is important to ensure that the device has short impulse response with minimum ringing. The annular CMUT array with outer diameter of 9.34 mm was evaluated in single-element and 100-element operating modes. Fig. 7(a) shows the impulse response of one element biased at 60 V of DC bias with 17 $V_{pp}$ sine-wave input at 6.2 MHz operating frequency, measured 3 mm from the surface of the CMUT array. A Gaussian function with full width at half maximum of 0.35 μs was multiplied to the original signal to remove the noise. The result shows that the length of the pulse was nearly 0.5 μs and the ringing was restricted immediately after a single response. The − 3 dB fractional bandwidth was 91%, which is within the bandwidth range of the conventional CMUT.

Among the 120 elements, we activated 100 elements to check the

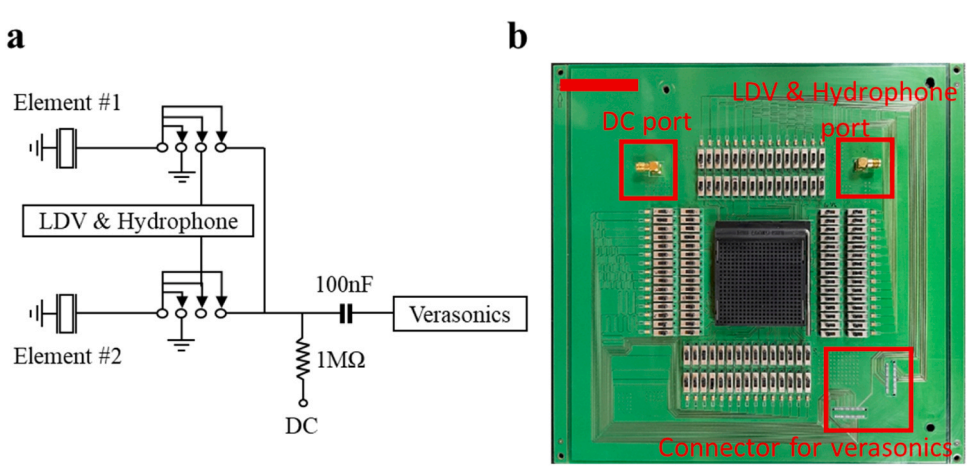


**Fig. 4.** Circuit system for annular array system. (a) Schematic and (b) photograph of printed circuit board. Scale bar is 50 mm.

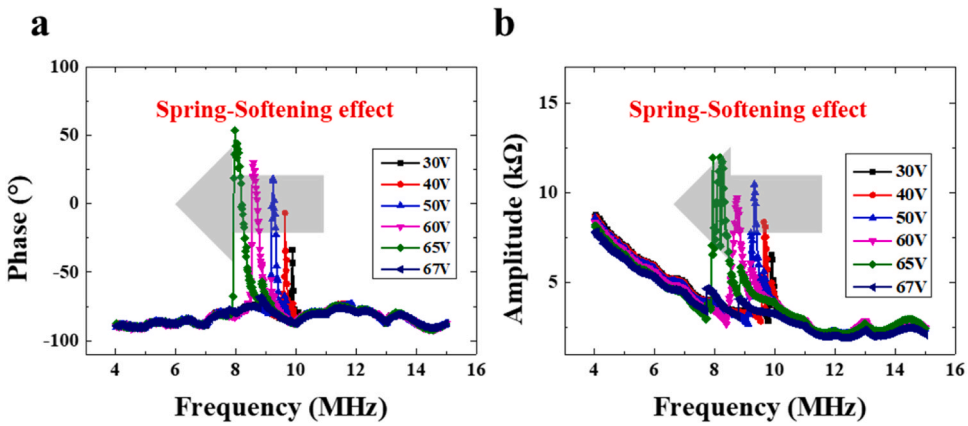


**Fig. 5.** Impedance measurement results of one element in the annular array. (a) Frequency vs. phase graph at different DC biases. (b) Frequency vs. amplitude graph at different DC biases.

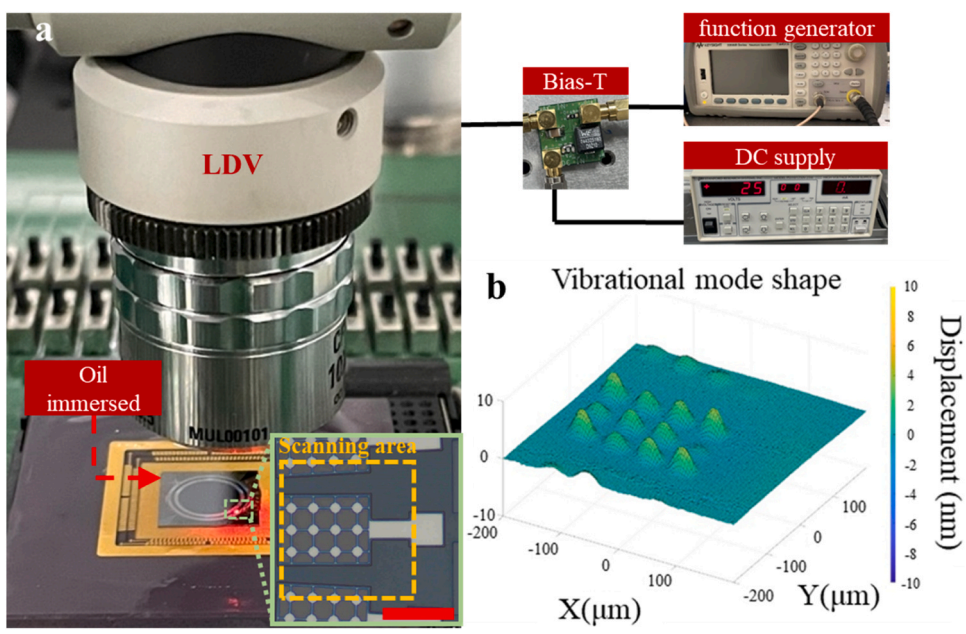


**Fig. 6.** (a) Schematic of setup for LDV measurement. Size of the scale bar is 200 μm. (b) 2D scan of membrane displacement with 40 $V_{dc}$, 5 $V_{pp}$, 6.2 MHz continuous sinusoidal signal.

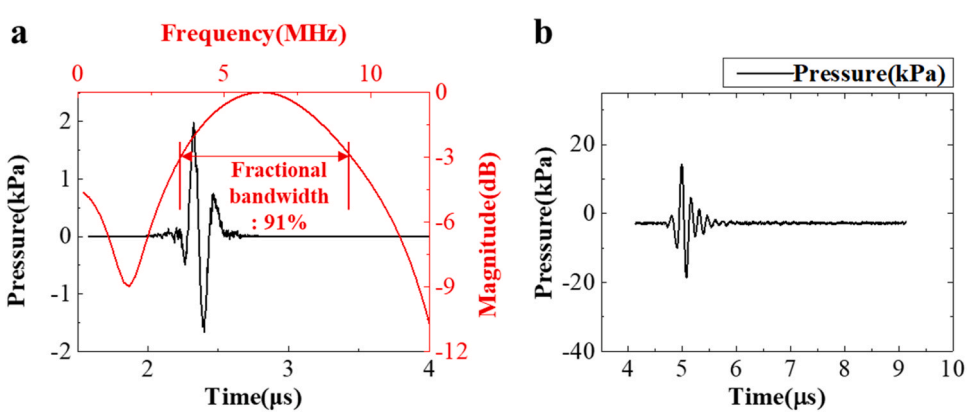


**Fig. 7.** Impulse response of CMUT activated in 1-element mode and 100-element mode. (a) Impulse response (black) and bandwidth (red) of 1 element. A Gaussian function was multiplied to remove the noise signal. (b) Impulse response of 100 elements.

acoustic pressure and signal length in the region where all signals from each element were focused due to avoid the beam distortion from the defective elements — in the defective 20 elements, the leakage current occurred. We aligned the hydrophone to the spot where the amplitude of the signal was the maximum; the signals from all elements were focused on this spot. Fig. 7(b) shows the impulse response of 100 elements at 40 V of DC bias with 5 $V_{pp}$ sine-wave input at 6.2 MHz operating frequency, measured 7 mm from the CMUT array. The amplitude of the single pulse generated by the 100 elements activated simultaneously was 32.7 kPa. However, the deviations among the elements caused ringing at the end of the single pulse. Nevertheless, the device remained attenuated within 1 μs in the 100-element operating mode.

## 4. Real-time 3D imaging

### 4.1. Imaging method

To demonstrate the proposed device, a Vantage 64 system was applied to control the delay of each element in the annular array of the CMUT. In this section, we adopted plane-wave imaging, which transmits a steered plane wave by adding a delay to each transducer. In physical terms, a plane wave is a type of coherent point source which has a focal point located at an infinite distance from the array plane. To achieve this, we applied an equal amount of delay to each pair of elements that were parallel to the axis perpendicular to the wave transmission direction. Specifically, we applied 30 different delays for each transmission. By steering the beam in the same range of X and Y directions, the number of beams was equal to the square of the number of transmissions in the X (or Y) direction. We found that the calculation tolerance of our system (Vantage 64, Verasonics Inc, USA) was limited to 289 (the square of 17) transmissions. Therefore, we set the number of transmissions to 289 to optimize system performance. To acquire sufficient data from the target, we steered the beam with a single step (1.25°) in the range of 20° for the X- and Y-axis. We additionally processed this image by adjusting the compression factor, displaying only the data above −30 dB intensity when compared with the maximum intensity. The processed volumetric data are depicted in three cross-sectional planes—XZ-, YZ-, and XY-plane.

### 4.2. Imaging demonstration using wire phantoms

Figs. 8 and 9 show three cross-sectional images and point spread functions of the wire phantoms immersed in oil. The device was excited by a 20 $V_{pp}$, 6.2 MHz sine pulse and 50 V of DC bias was applied for pre-bending of the membrane. Among the 120 elements in the annular array, we activated 100 elements to prevent electrical leakage from the defective elements. As shown in Fig. 8, we aligned three fishing wires with 380 μm diameter, 25 mm away from the center of the bottom of the tank, at − 10°, 0°, and 10° from the center of the transducer in the XZ-plane. In the XY-plane, we set the depth of the image plane as 28 mm from the device considering the water tank thickness of 3 mm. As the only wire that overlapped with the YZ- and XY-plane was the wire at the center of the tank, we could observe only one line in the YZ-plane (Fig. 8 (b)) and XY-plane (Fig. 8(c)). As the focus of the ultrasound wave was the strongest at the center of the proposed device, the wire at this position was displayed most sharply (Fig. 8(a)). Moreover, the wavelength

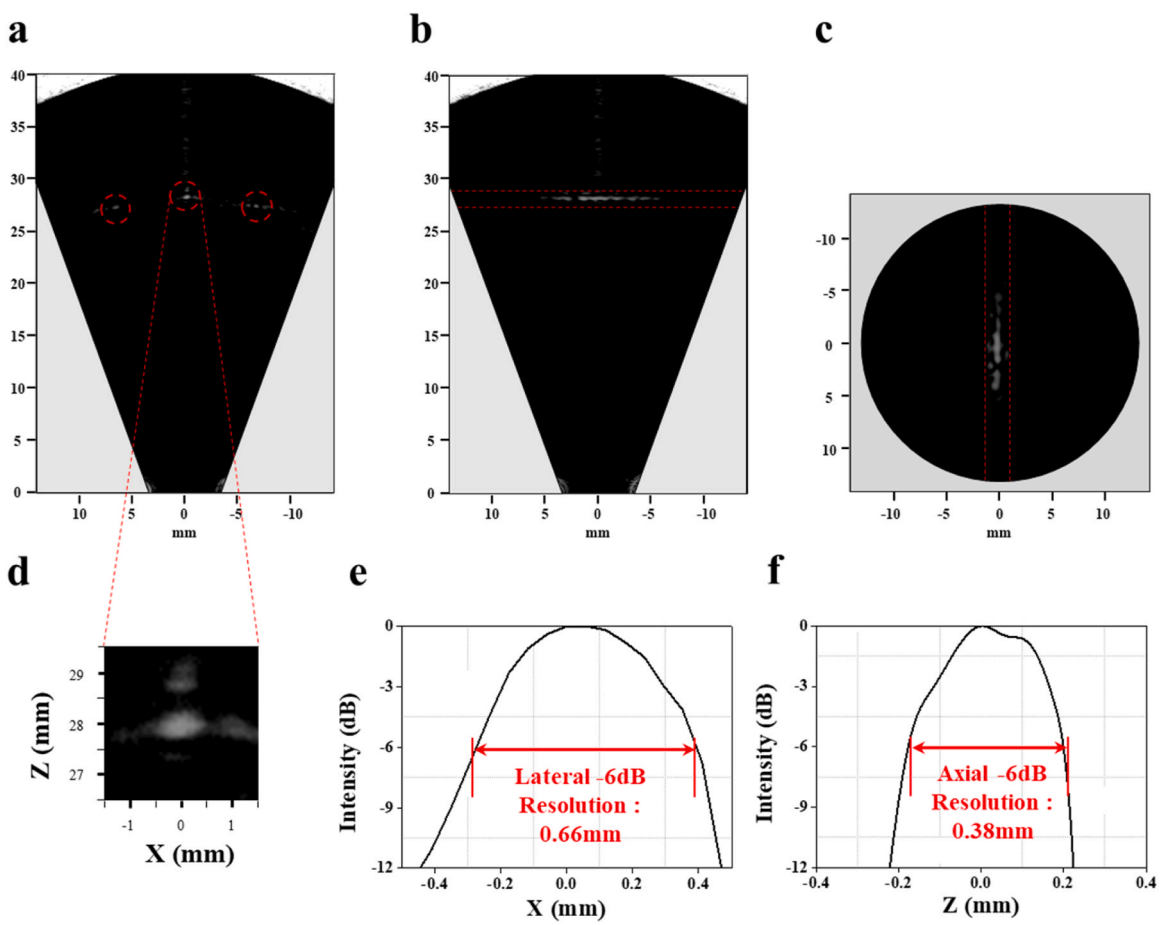


**Fig. 8.** Imaging demonstration of wire phantoms positioned at 28 mm distance from the annular CMUT array. From the left, image in (a) XZ-plane, (b) YZ-plane, (c) XY-plane (imaging depth: 28 mm). (d) Captured image of the wire. (e) Point spread function (lateral direction): − 6 dB resolution was 0.66 mm. (f) Point spread function (axial direction): − 6 dB resolution was 0.38 mm.

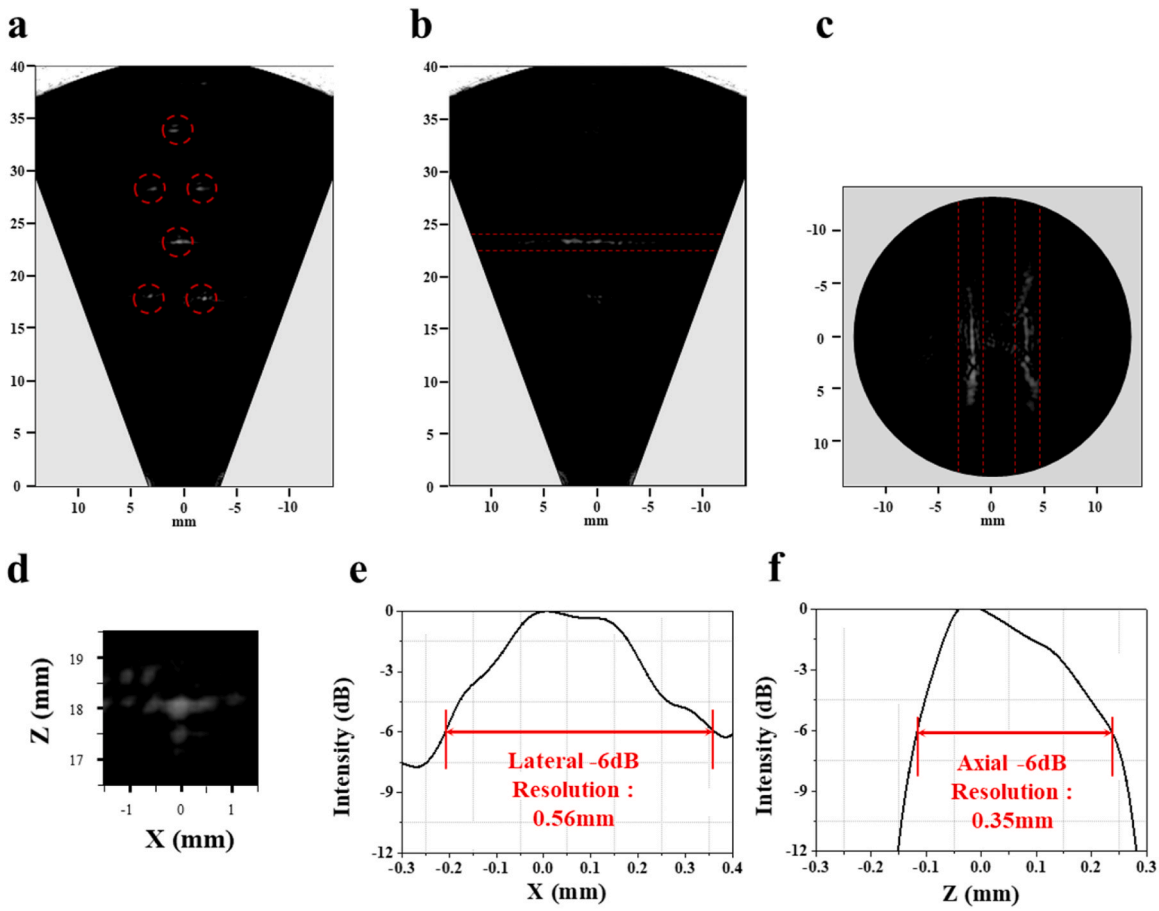


**Fig. 9.** Imaging demonstration of wire phantoms positioned at various distances from the annular CMUT array. From the left, image in (a) XZ-plane, (b) YZ-plane, (c) XY-plane (imaging depth: 18 mm). (d) Captured image of the wire. (e) Point spread function (lateral direction): − 6 dB resolution was 0.56 mm. (f) Point spread function (axial direction): − 6 dB resolution was 0.35 mm.

of the transmitted wave (238 μm) was shorter than the diameter of the wire (380 μm), which may have caused reflection of the ultrasound waves at the inner boundary of the wire. This reflected signal was displayed immediately behind the main signal of the wire at the center of the proposed device. We additionally calculated a point spread function from the captured image of the wire positioned 28 mm away from the proposed device (Fig. 8(d)). The point spread function is a method to determine the lateral and axial resolutions of the annular CMUT array. The sharper the spread function plot, the better is resolution of the proposed device. From the point spread functions in the lateral and axial directions (Fig. 8(e), (f)), we found that the − 6 dB lateral and axial resolutions were 0.66 mm and 0.38 mm, respectively.

In Fig. 9, we used six instead of three wires as the target phantoms. The wires were positioned 18–33 mm from the proposed device (Fig. 9 (a)). All six wires were detected at the same positions as the real phantoms. Although two lines overlapped with the YZ-plane at 23 mm and 33 mm, only one wire positioned at 23 mm from the proposed device was detected in the image in the YZ-plane (Fig. 9(b)). The slightly shifted position of the wire at 33 mm and blocking effect of the wire positioned at 23 mm were the main reasons for the failure to detect the wire at 33 mm. The blocking effect was also observed in wires positioned at 28 mm from the proposed device; this was expected owing to increased attenuation when compared with the wires at 18 mm from the proposed device. In the case of the XY-plane, we set the depth of the image plane as 18 mm from the proposed device (Fig. 9(c)). The two lines shown in the XY-plane verify that the plane at a distance of 18 mm from the device was successfully imaged. The point spread function of the wires positioned at 18 mm was also calculated from the captured image (Fig. 9(d)). The point spread function in the lateral direction shows the − 6 dB lateral resolution as 0.56 mm (Fig. 9(e)). The 6 dB axial resolution was 0.35 mm (Fig. 9(f)). The wire positioned at 18 mm shows narrower lateral and axial resolutions when compared with the result in Fig. 8. The higher SNR of the signal and narrower beam width due to the proximity are the main reasons for the differences in the lateral and axial resolutions.

From the above results of wire imaging, we concluded that the lateral resolution of the focused region formed by the plane wave was sufficiently narrow to detect a 380 μm target. The results are particularly encouraging, considering that this image was obtained without an amplifier.

### 4.3. Comparison of imaging methods

Table 2 lists the normalized frame rates of the CPA, SPA, and plane-wave imaging. Real-time volumetric imaging was possible only for the SPA and plane-wave imaging owing to the low data acquisition rate of the CPA. In a previous study, the fact that frame rate is inversely proportional to the number of processed voxels was verified from the measurement of frame rates with different number of voxels [15]. For precise comparison of the frame rate, we modified the imaging depth to 17 mm to obtain a voxel count comparable to that of the SPA. The SPA exhibits a frame rate of 8.5 fps for reconstructing two cross-sectional planes with 45,602 voxels whereas plane-wave imaging exhibits a frame rate of 1.49 fps for reconstructing three cross-sectional planes with 45,702 voxels. Although the plane-wave imaging method transmits four times the number of waves at a deeper imaging depth, the frame

**Table 2**
Comparison of imaging methods.

| | CPA | SPA | Plane wave imaging (Imaging depth = 40 mm) | Plane wave imaging[e] (Imaging depth = 17 mm) |
|---|---|---|---|---|
| Frame per second | Offline[a] | 8.5 | 0.45 | 1.49 |
| Number of transmit | 16471[b] | 64 | 289 | 289 |
| Voxel size[c] | 0.1 mm × 0.23 mm× 0.23 mm | 0.1 mm × 0.23 mm× 0.23 mm | 0.12 mm × 0.12 mm× 0.12 mm | 0.12 mm × 0.12 mm × 0.12 mm |
| Number of voxels | 45602 | 45602[d] | 158751 | 45702 |
| Lateral resolution[f] | 0.64 mm (wire target at 13 mm depth) | 0.77 mm (wire target at 13 mm depth) | 0.56 mm (wire target at 18 mm depth) | 0.56 mm (wire target at 18 mm depth) |
| Imaging depth | 26 mm | 26 mm | 40 mm | 17 mm |

[a] CPA was not tested in real-time mode.
[b] Beam-sampling interval of 1° was assumed in both θ- and φ-directions with viewing angle of 90° for θ and 180° for φ.
[c] For CPA and SPA, the width and length of the voxel were calculated at 1.3 cm depth.
[d] In a previous study, the constant R-image was processed offline for compounding [14].
[e] For precise comparison with the results of the previous study, we set the number of voxels to the same value as applied for SPA.
[f] Lateral resolution of the previous study was calculated by multiplying the target depth (mm) with the FWHM of the line spread function (radian).

rate of the plane-wave imaging method was comparable to that of SPA imaging. As the size of the voxel was non-uniform in the previous study [15], the lateral dimensions of the voxel in the SPA and CPA were calculated at the halfway imaging depth of 13 mm. The non-uniformity of the voxel caused lower lateral resolution with increase in the imaging depth. As shown in Table 2, the lateral resolution of SPA imaging in the previous study was 770 μm, i.e., higher than 560 μm of plane-wave imaging. In comparison with the results of the previous study, plane-wave imaging with a uniform voxel size achieved a uniform lateral resolution independent of the imaging depth.

## 5. Conclusion

In this study, we demonstrated 3D plane-wave imaging using an annular CMUT array. The images in the XZ-, YZ-, and XY-planes verified that the device successfully collects the volumetric data of the targeting region. Although the side lobes in the imaging result appeared higher as the phantom surpassed the steering range of the beam, the main lobe remained distinguishable. The point spread function of the annular CMUT array shows that the − 6 dB lateral and axial resolutions were sufficiently narrow to detect wire targets with a 380 μm diameter. In particular, it is encouraging that plane-wave imaging provides higher frame rate when compared with the SPA, even for a higher number of transmissions. Given that the wires with 380 μm diameter were successfully detected, we concluded that the focused region in the plane wave formed by the annular array can also provide distinguishable phantom images. In addition, the comparison of frame rate among the different imaging methods proved that plane-wave imaging using the annular CMUT array has comparable frame rate to those of CPA and SPA imaging and improved lateral resolution. We concluded that plane-wave imaging using an annular array is suitable for real-time 3D imaging and delivers improved frame rate when compared with those of SPA and CPA imaging in a previous study [15].

Future research can focus on alleviating the side lobe by decreasing the element-to-element distance to less than λ/2. We also grounded 20 underperforming elements to achieve a more uniform performance. We expect to increase the SNR and decrease the side lobes by decreasing the pitch size and limiting the element-to-element performance deviation. We grouped two elements into one channel to connect with a 64-channel Vantage 64. However, we expect to achieve superior control of the beam and better lateral resolution with Vantage 128, which will enable the individual control of 120 elements.

## Funding

This study was supported by the Bio & Medical Technology Development Program of the National Research Foundation (NRF) funded by the Ministry of Science & ICT (No. NRF-2018M3A9G5075749). This work was also supported in part by a Korea Medical Device Development Fund grant funded by the Korean government (Ministry of Science and ICT, Ministry of Trade, Industry and Energy, Ministry of Health & Welfare, and Ministry of Food and Drug Safety) (No. 202011D01 and No. KMDF_PR_20200901_0145–2021). Also, this work was supported by the Nanomedical Devices Development Project of NNFC in 2022 (No. 1711160154).

## CRediT authorship contribution statement

**Young Seok Kwon**: Methodology, Data curation, Visualization, Writing – original draft. **Hae Youn Kim**: Methodology, Data curation, Writing – original draft. **Dong-Hyun Kang**: Methodology, Data curating, Writing – original draft. **Dong Hun Kim**: Data curating, Writing – original draft. **Jae-Woong Jeong**: Data curation, Investigation, Supervision, Writing – review & editing. **Byung Chul Lee**: Conceptualization, Data curation, Investigation, Supervision, Project administration, Funding acquisition, Writing – review & editing.

## Declaration of Competing Interest

The authors declare that they have no known competing financial interests or personal relationships that could have appeared to influence the work reported in this paper.

## Data Availability

Data will be made available on request.

## Acknowledgments

The authors would like to especially thank Micro-Nano Fab Center at Korea Institute of Science and Technology (KIST) for their dedicated contribution on the CMUT device fabrication.

## References

[1] Y. Wang, D.N. Stephens, M. O'Donnell, Optimizing the beam pattern of a forward-viewing ring-annular ultrasound array for intravascular imaging, IEEE Trans. Ultrason. Ferroelect. Freq. Contr. 49 (2002) 1652–1664, https://doi.org/10.1109/TUFFC.2002.1159845.
[2] J.L. Sanders, A.O. Biliroğlu, I.G. Newsome, O.J. Adelegan, F.Y. Yamaner, P. A. Dayton, O. Oralkan, A handheld imaging probe for acoustic angiography with an ultrawideband capacitive micromachined ultrasonic transducer (CMUT) array, IEEE Trans. Ultrason. Ferroelect. Freq. Contr. 69 (2022) 2318–2330, https://doi.org/10.1109/TUFFC.2022.3172566.
[3] S. Sadeghpour, S.V. Joshi, C. Wang, M. Kraft, Novel phased array piezoelectric micromachined ultrasound transducers (pMUTs) for medical imaging, IEEE Open J. Ultrason., Ferroelectr., Freq. Control vol. 2 (2022) 194–202, https://doi.org/10.1109/OJUFFC.2022.3207128.

[4] I.O. Wygant, X. Zhuang, D.T. Yeh, O. Oralkan, A.S. Ergun, M. Karaman, B.T. Khuri-Yakub, Integration of 2D CMUT arrays with front-end electronics for volumetric ultrasound imaging, IEEE Trans. Ultrason. Ferroelect. Freq. Contr. 55 (2008) 327–342, https://doi.org/10.1109/TUFFC.2008.652.
[5] A. Bhuyan, J.W. Choe, B.C. Lee, I.O. Wygant, A. Nikoozadeh, O. Oralkan, B. T. Khuri-Yakub, Integrated circuits for volumetric ultrasound imaging with 2-D CMUT arrays, IEEE Trans. Biomed. Circuits Syst. 7 (2013) 796–804, https://doi.org/10.1109/TBCAS.2014.2298197.
[6] I.O. Wygant, N.S. Jamal, H.J. Lee, A. Nikoozadeh, O. Oralkan, M. Karaman, B. T. Khuri-yakub, An integrated circuit with transmit beamforming flip-chip bonded to a 2-D CMUT array for 3-D ultrasound imaging, IEEE Trans. Ultrason. Ferroelect. Freq. Contr. 56 (2009) 2145–2156, https://doi.org/10.1109/TUFFC.2009.1297.
[7] D.E. Dausch, J.B. Castellucci, D.R. Chou, O.T. von Ramm, Theory and operation of 2-D array piezoelectric micromachined ultrasound transducers, IEEE Trans. Ultrason. Ferroelectr. Freq. Control vol. 55 (11) (2008) 2484–2492, https://doi.org/10.1109/TUFFC.956.
[8] Q. Duan, S. Homma, A.F. Laine, Analysis of 4D ultrasound for dynamic measures of cardiac function, 2007 IEEE Ultrason. Symp. . Proc. (2007) 1492–1495, https://doi.org/10.1109/ULTSYM.2007.375.
[9] H. Chen, Z. Liu, Y. Gong, B. Wu, C. He, Evolutionary strategy-based location algorithm for high-resolution lamb wave defect detection with sparse array, IEEE Trans. Ultrason. Ferroelect. Freq. Contr. 68 (2021) 2277–2293, https://doi.org/10.1109/TUFFC.2021.3060094.
[10] T. Zhang, W. Zhang, X. Shao, Y. Yang, Z. Wang, Y. Wu, Y. Pei, A study on capacitive micromachined ultrasonic transducer periodic sparse array, Micromachines 12 (2021) 684, https://doi.org/10.3390/mi12060684.
[11] J. Wang, Z. Zheng, J. Chan, J.T.W. Yeow, Capacitive micromachined ultrasound transducers for intravascular ultrasound imaging, Microsyst. Nanoeng. 6 (2020) 73, https://doi.org/10.1038/s41378-020-0181-z.
[12] D.T. Yeh, O. Oralkan, I.O. Wygant, M. O'Donnell, B.T. Khuri-Yakub, 3-D ultrasound imaging using a forward-looking CMUT ring array for intravascular/intracardiac applications, IEEE Trans. Ultrason. Ferroelect. Freq. Contr. 53 (2006) 1202–1211, https://doi.org/10.1109/TUFFC.2006.1642519.
[13] S.J. Norton, Annular array imaging with full-aperture resolution, J. Acoust. Soc. Am. 92 (1992) 3202–3206, https://doi.org/10.1121/1.404169.
[14] F.L. Degertekin, R.O. Guldiken, M. Karaman, Annular-ring CMUT arrays for forward-looking IVUS: Transducer characterization and imaging, IEEE Trans. Ultrason. Ferroelect. Freq. Contr. 53 (2006) 474–482, https://doi.org/10.1109/TUFFC.2006.1593387.
[15] J.W. Choe, O. Oralkan, A. Nikoozadeh, M. Gencel, D.N. Stephens, M. O'Donnell, D. J. Sahn, B.T. Khuri-Yakub, Volumetric real-time imaging using a CMUT ring array, IEEE Trans. Ultrason. Ferroelect. Freq. Contr. 59 (2012) 1201–1211, https://doi.org/10.1109/TUFFC.2012.2310.
[16] G. Montaldo, M. Tanter, J. Bercoff, N. Benech, M. Fink, Coherent plane-wave compounding for very high frame rate ultrasonography and transient elastography, IEEE Trans. Ultrason. Ferroelectr. Freq. Control vol. 56 (3) (2009) 489–506, https://doi.org/10.1109/TUFFC.2009.1067.
[17] M. Maadi, C. Ceroici, R.J. Zemp, Dual-frequency CMUT arrays for multiband ultrasound imaging applications, IEEE Trans. Ultrason. Ferroelect. Freq. Contr. 68 (2021) 2532–2542, https://doi.org/10.1109/TUFFC.2021.3062071.
[18] G. Gurun, M. Hochman, P. Hasler, F.L. Degertekin, Thermal-mechanical-noise-based CMUT characterization and sensing, IEEE Trans. Ultrason. Ferroelect. Freq. Contr. 59 (2012) 1267–1275, https://doi.org/10.1109/TUFFC.2012.2317.
[19] O.J. Adelegan, Z.A. Coutant, X. Zhang, F.Y. Yamaner, O. Oralkan, Fabrication of 2D capacitive micromachined ultrasonic transducer (CMUT) arrays on insulating substrates with through-wafer interconnects using sacrificial release process, J. Micro Syst. 29 (2020) 553–561, https://doi.org/10.1109/JMEMS.2020.2990069.
[20] M. Wang, J. Chen, Volumetric flow measurement using an implantable CMUT array, IEEE Trans. Biomed. Circuits Syst. 5 (2011) 214–222, https://doi.org/10.1109/TBCAS.2010.2095848.
[21] N. Tas, T. Sonnenberg, H. Jansen, R. Legtenberg, M. Elwenspoek, Stiction in surface micromachining, J. Micromech. Microeng. 6 (1996) 385–397, https://doi.org/10.1088/0960-1317/6/4/005.
[22] D.-S. Lin, X. Zhuang, S.H. Wong, A.S. Ergun, M. Kupnik, B.T. Khuri-Yakub, 6F-5 characterization of fabrication related gap-height variations in capacitive micromachined ultrasonic transducers. Proceedings of the 2007 IEEE Ultrasonics Symposium Proceedings, IEEE, New York, NY, USA, 2007, pp. 523–526.
[23] O. Oralkan, B. Bayram, G.G. Yaralioglu, A.S. Ergun, M. Kupnik, D.T. Yeh, I. O. Wygant, B.T. Khuri-Yakub, Experimental characterization of collapse-mode CMUT operation, IEEE Trans. Ultrason. Ferroelect. Freq. Contr. 53 (2006) 1513–1523, https://doi.org/10.1109/TUFFC.2006.1665109.

**Young Seok Kwon** is a M.S candidate in Electrical Engineering at Korea Advanced Institute of Science and Technology (KAIST) and a researcher at Korea Institute of Science and Technology (KIST). He is currently doing research on fabricating novel micromachined ultrasonic transducers including CMUT.

**Hae Youn Kim** received the B.S degree in Biomedical Engineering from Dongguk University in 2020 and the M.S degree in Electrical Engineering from Yonsei University in 2022. She is a researcher at Korea Institute of Science and Technology (KIST), Seoul, Korea.

**Dong-Hyun Kang** received the B.S. (2010), M.S. (2013) and Ph.D. (2019) degree in Mechanical Engineering from Yonsei University, Seoul, Korea. In 2018, he joined Korea Institute of Science and Technology (KIST) as a specialist in the Micro Nano Fab Center. He is currently working on Bionics Research Center as Post Doctoral Researcher (Dr. Byung Chul Lee's group). His research interests include N/MEMS, ultrasound transducers, and their biological applications.

**Dong Hun Kim** obtained the B.S degree in Electrical and Computer Engineering with an additional B.S degree in Biomedical Engineering from Carnegie Mellon University in 2019. He then obtained the M.S. degree in Electrical and Computer Engineering from Carnegie Mellon University in 2020. He currently works as a researcher at the Korea Institute of Science and Technology (KIST)'s Bionics Research Center on medical ultrasound imaging.

**Jae-Woong Jeong** is an Associate Professor in Electrical Engineering at Korea Advanced Institute of Science and Technology (KAIST). He received his BS degree from the University of Texas at Austin in 2005, and MS and PhD degrees from Stanford University in 2008 and 2012, respectively, all in electrical engineering. He worked as a postdoctoral research associate in Frederick Seitz Materials Research Laboratory at the University of Illinois at Urbana-Champaign from 2012 to 2014, and as an Assistant Professor in Electrical, Computer & Energy Engineering at University of Colorado Boulder from 2015 to 2017. Dr. Jeong's research focus is in the future generation bio-integrated electronics and systems for advanced healthcare and brain research, based on unusual materials, flexible/stretchable electronics and N/MEMS technologies.

**Byung Chul Lee** received the B.S. degree (Summa Cum Laude) from Korea University, the M.S. degree from Korea Advanced Institute of Science and Technology (KAIST), and the Ph.D. degree from Stanford University, all in electrical engineering, in 2003, 2005, and 2015, respectively. He is now working as a principal research scientist in Bionics Research Center at KIST, Seoul, Korea. Also, he is now an associate professor in Division of Bio-Medical Science and Technology at University of Science and Technology (UST), Seoul, Korea. He also joined as an associate professor in KHU-KIST Department of Converging Science and Technology, Kyung Hee University, Seoul, Korea in 2022. His research interests include MEMS/NEMS technology for diverse biomedical applications such as bioelectronics, biosensors, micro-nanofluidics, micro-nanofabrications, and novel micromachined ultrasonic transducers including its ASIC and integrated systems.